Response of Atmospheric Convection to Vertical Wind Shear: Cloud-System-Resolving Simulations with Parameterized Large-Scale Circulation. Part II: Effect of Interactive Radiation

USAMA ANBER

Lamont-Doherty Earth Observatory, Palisades, and Department of Earth and Environmental Sciences, Columbia University, New York, New York

SHUGUANG WANG

Department of Applied Physics and Applied Mathematics, Columbia University, New York, New York

ADAM SOBEL

Lamont-Doherty Earth Observatory, Palisades, and Department of Applied Physics and Applied Mathematics, and Department of Earth and Environmental Sciences, Columbia University, New York, New York

(Manuscript received 12 June 2015, in final form 27 August 2015)

ABSTRACT

The authors investigate the effects of cloud–radiation interaction and vertical wind shear on convective ensembles interacting with large-scale dynamics in cloud-resolving model simulations, with the large-scale circulation parameterized using the weak temperature gradient approximation. Numerical experiments with interactive radiation are conducted with imposed surface heat fluxes constant in space and time, an idealized lower boundary condition that prevents wind–evaporation feedback. Each simulation with interactive radiation is compared to a simulation in which the radiative heating profile is held constant in the horizontal and in time and is equal to the horizontal-mean profile from the interactive-radiation simulation with the same vertical shear profile and surface fluxes. Interactive radiation is found to reduce mean precipitation in all cases. The magnitude of the reduction is nearly independent of the vertical wind shear but increases with surface fluxes. Deep shear also reduces precipitation, though by approximately the same amount with or without interactive radiation. The reductions in precipitation due to either interactive radiation or deep shear are associated with strong large-scale ascent in the upper troposphere, which more strongly exports moist static energy and is quantified by a larger normalized gross moist stability.

1. Introduction

Radiative feedbacks have been shown to contribute to the dynamics of tropical disturbances on a range of time scales. The phenomena influenced by these feedbacks include tropical cyclogenesis (e.g., Bu et al. 2014; Hakim 2013) and intraseasonal variability (e.g., Raymond 2001; Bony and Emanuel 2005; Kim et al. 2011; Sobel and Maloney 2013) and have been found in observations (e.g., Lin and Mapes 2004; Sobel et al. 2014) as well as idealized numerical modeling studies (e.g., Raymond 2001; Grabowski and Moncrieff 2002; Bony and Emanuel 2005; Wing and Emanuel 2014).

By absorbing longwave radiation and reemitting it to space at lower temperatures, clouds and water vapor warm the troposphere. Locally, regions of deep convection experience a strong reduction in the net radiative cooling compared to adjacent clear-sky regions. At the top of the atmosphere, this longwave warming is often largely (though imperfectly; Lin and Mapes 2004), offset by shortwave anomalies due to the enhanced albedo of deep clouds (e.g., Ramanathan et al. 1989; Hartmann et al. 2001), so that the effect of high tropical clouds on the long-term climate is modest. However, the longwave effect is felt immediately in the atmosphere, while the compensating shortwave effect is felt largely at

Corresponding author address: Usama Anber, Lamont-Doherty Earth Observatory, 61 Route 9W, Palisades, NY 10964.
E-mail: uanber@ldeo.columbia.edu

DOI: 10.1175/JAS-D-15-0151.1

the surface. If the surface is ocean, the heat capacity of the ocean mixed layer can delay the surface response enough that on short time scales, the positive feedback in the atmosphere dominates. By acting as a source of column-integrated moist static energy in a location where a positive anomaly in column-integrated moist static energy is already present, this longwave radiative feedback is positive and can organize tropical convection on a range of scales, including intraseasonal (Raymond 2001; Sobel and Gildor 2003; Grabowski and Moncrieff 2002; Bretherton et al. 2005; Wing and Emanuel 2014; Emanuel et al. 2014; Tobin et al. 2013; Chikira 2014).

We expect the effectiveness of cloud–radiative feedbacks to be related to the horizontal extent, vertical structure, and microphysical properties of the cloud field. These cloud properties, in turn, are influenced by a number of environmental factors. Vertical wind shear is an important such factor, in that we expect it to play a significant role in the organization of convective cloud systems on the mesoscale. In this study, we describe experiments designed to isolate the effects of interactive radiation and vertical shear, together and separately, on tropical oceanic convection.

In the first part of this study (Anber et al. 2014, hereafter Part I), we performed cloud-system resolving model (CRM) simulations in which we prescribed both surface fluxes and column radiative heating and introduced a background vertical wind shear of different strengths as a control parameter. We found that under otherwise identical large-scale conditions, the precipitation can change significantly as a result of the wind shear influence as the shear organizes the convective systems into squall-line-like structures. These structures influence the convective heating and large-scale vertical motion profiles, with the relationship between heating and large-scale vertical motion parameterized in Part I by the weak temperature gradient (WTG) approximation. The different vertical motion profiles lead to different mean precipitation rates for the same export of moist static energy (with that export fixed in the experiments of Part I by the imposed surface fluxes and radiative cooling)—a relationship quantified by the normalized gross moist stability.

In this sequel paper, we perform similar model integrations, again studying the influence of vertical wind shear on tropical convection, but now with interactive radiative heating. The results are then compared to those obtained from otherwise identical experiments in which the radiative heating is prescribed to have the same profile, in the time and horizontal mean, as the interactive-radiation simulations.

Our simulation design is such that we are not studying the most direct aspects of the radiative feedback on convective organization, in which the radiative heating itself changes on the large scale (represented in our simulations by the horizontal and time mean over the domain). This direct radiative feedback, relevant to tropical disturbances, can be estimated straightforwardly, from observations or global model simulations, as the column-integrated radiative heating anomaly per unit anomaly in column water vapor, precipitation, or other metric of convective activity on the space and time scale of interest (e.g., Bretherton and Sobel 2002; Su and Neelin 2002; Lin and Mapes 2004). Rather, we investigate the more indirect effects that result not from the change in the areally averaged radiative heating, but from the effects that interactive radiation may have on cloud structure and dynamics, holding the large-scale-mean radiative heating profile fixed. That is, we compare interactive- and fixed-radiation simulations in which the radiative heating is the same in the horizontal and time mean. Interactive-radiation effects then change the cloud system structure and horizontal-mean latent heating and influence the export of moist static energy via changes in the large-scale vertical motion profile associated with those latent heating changes. We find that these effects can be quite significant. We are not aware of any previous documentation of them.

To facilitate our focus on the vertical shear influence and cloud–radiative interaction, we prescribe surface turbulent heat fluxes (Part I; Anber et al. 2015). This eliminates surface flux feedbacks that would occur if the lower boundary were taken to be at fixed sea surface temperature (SST). With varying vertical shear, changes in momentum transport to the surface can change surface winds from one simulation to the next, inducing strong surface turbulent flux feedbacks under fixed SST. These feedbacks are not of interest here, so we eliminate them by prescribing surface turbulent heat fluxes directly. We have also conducted simulations with a slab ocean model; these increase the size of the parameter space and the range of possible model behavior enough that we will report on them in a separate study.

After describing the model and experiment design in section 2, we present the results in section 3. We summarize in section 4.

2. Model and experiment design

The model used here is the Weather Research and Forecast (WRF) Model, version 3.3, in three spatial dimensions with doubly periodic lateral boundary conditions with the same physical parameterization schemes used in Part I. The experiments are conducted with Coriolis parameter $f = 0$. The horizontal domain size is $192 \times 192\,\mathrm{km}^2$ with a grid spacing of 2 km. There are 50

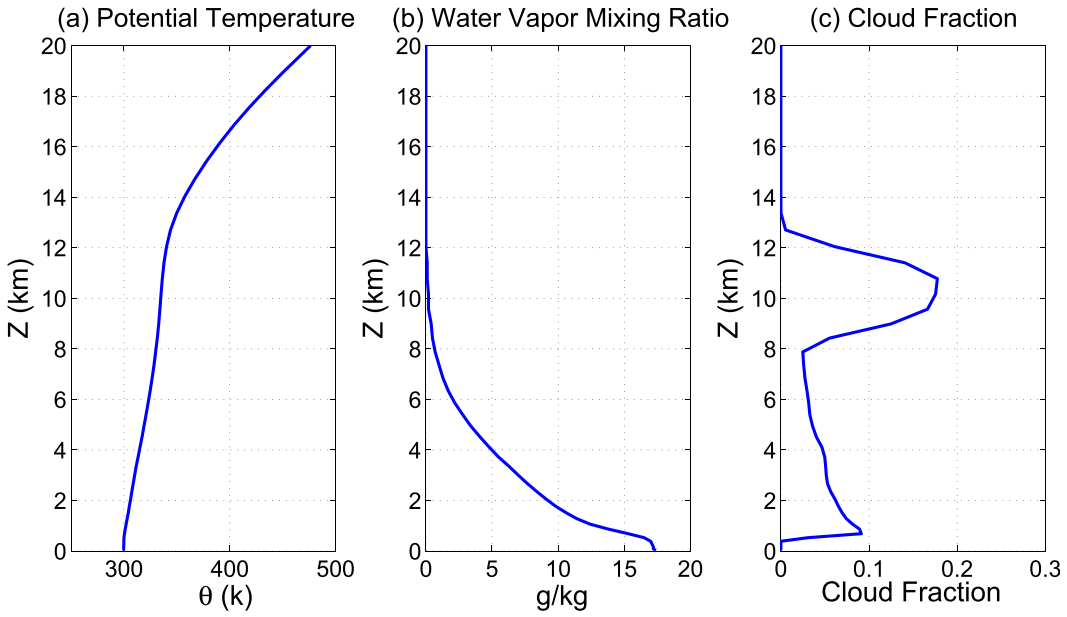

FIG. 1. Equilibrium vertical profiles of (a) potential temperature, (b) water vapor mixing ratio, and (c) cloud fraction from the RCE simulation.

vertical levels total, with the top level at 22 km, and 10 levels in the lowest 1 km. Large-scale circulation is parameterized using WTG approximation (Sobel and Bretherton 2000; Raymond and Zeng 2005) as

$$W(z) = \begin{cases} \dfrac{1}{\tau}\dfrac{\theta - \theta_0}{\partial\theta/\partial z}, & z \geq h \\ \dfrac{z}{h} W(h), & z < h \end{cases}, \qquad (1)$$

where θ is the domain-mean potential temperature, θ_0 is the reference temperature (from a radiative–convective equilibrium run; see below), h is the height of the boundary layer determined internally by the boundary layer scheme, and τ is the relaxation time scale and can be thought of as the time scale over which gravity waves propagate out of the domain, taken here to be 3 h. For a more complete explanation of the experimental design and implementation of WTG in the WRF Model, the reader is referred to Part I, but we state key details here.

All experiments are integrated more than 40 days to achieve statistical equilibrium, and analysis of the output is conducted on the last 20 days, during which the simulations have reached statistical equilibrium.

To obtain the reference temperature profile required for WTG, we follow a standard procedure (e.g., Sobel and Bretherton 2000; Raymond and Zeng 2005; Wang and Sobel 2011). We first perform a radiative–convective equilibrium (RCE) experiment at a fixed SST of 28°C, with interactive radiation, specified surface turbulent heat fluxes of 100 W m^{-2}, and no mean vertical shear. This experiment reaches equilibrium in about 60 days. Results from this experiment are averaged over the last 10 days after equilibrium to obtain statistically equilibrated temperature and moisture profiles. Figure 1 shows the resulting vertical profiles of potential temperature (Fig. 1a), moisture (Fig. 1b), and cloud fraction (Fig. 1c). These profiles are then used to initialize runs with parameterized large-scale dynamics, and the temperature profile is used as the target profile against which perturbations are computed in the WTG runs.

For our experiments with interactive radiation, the NCAR Community Atmosphere Model (CAM3.0) shortwave and longwave radiation schemes (Collins et al. 2004) are used. Diurnal and seasonal cycles are removed and the top of the atmosphere incident solar flux is set to 400 W m^{-2}.

For WTG runs without vertical wind shear, we prescribe total turbulent surface fluxes of heat and moisture at three different values: low (140 W m^{-2}), moderate (180 W m^{-2}), and high (220 W m^{-2}); these variations are achieved holding the sensible heat flux fixed at 20 W m^{-2} while the latent heat flux takes on values of 120, 160, and 200 W m^{-2}, respectively. These values approximately span the range between active and suppressed phases of the Madden–Julian oscillation (e.g., Shinoda et al. 1998; Sobel et al. 2014; de Szoeke et al. 2015).

We constrain the vertical wind shear by relaxing the horizontal-mean zonal wind toward a prescribed profile with a time scale of 1 h, as in Part I. The shear profile is

linear varying depth over three layers: shallow (1500 m), midlevel (4500 m), and deep (12 000 m). In each case, the target wind speed at the top of the shear layer is constant at 20 m s^{-1}, and we keep it zero at the surface (see Fig. 1 of Part I). (We have also conducted experiments with larger shears, using zonal wind values at shear layer top of 30 and 40 m s^{-1}. The results of interest to this study are qualitatively similar to those from the experiments using 20 m s^{-1}, so we omit the results with larger shears and focus on the effects of varying shear depth rather than magnitude with shear layer top zonal wind held at 20 m s^{-1}.) Surface fluxes for this set of experiments are held fixed at 140, 180, and 220 W m^{-2} but we show results from the case of 180 W m^{-2} only since the results from the other cases are similar. Clouds and water vapor then evolve freely and strongly influence the radiative heating profile.

The time- and domain-averaged radiative heating profiles for this set of experiments are shown in Fig. 2a for the unsheared environment with different surface fluxes and Fig. 2b for different shear depths with intermediate surface fluxes. For either low surface fluxes or shallow shear, there is a cooling throughout almost the whole atmospheric column that reaches 1 K day^{-1} in the upper troposphere. For higher surface fluxes or deeper shear, there is a layer of significant radiative heating in the mid- to upper troposphere, exceeding 5 K day^{-1} for high surface fluxes. Above 10 km, there is a sharp drop in the radiative heating profile owing to the strong emission of longwave radiation from cloud top, with radiative cooling exceeding 10 K day^{-1} for strong surface fluxes or deep shear.

To compare the effect of interactive radiation on the cumulus ensemble interacting with the parameterized large-scale dynamics, we perform a set of experiments identical to those described above except that we prescribe the radiative heating profile in Fig. 2 and keep it constant in both the horizontal and time. The time- and domain-averaged radiative heating is the same with either fixed or interactive radiation. As surface fluxes are already fixed, this means that both the equilibrated time- and horizontal-mean column-integrated moist static surface fluxes and net radiative heating are identical in pairs of interactive- and fixed-radiation experiments. The radiative heating can and does differ between the two members of each pair at individual points in space and time, but as the radiative heating is a linear term in the moist static energy budget, only its time and horizontal mean enters the time- and horizontal-mean budget. Any differences in the time- and horizontal-mean column moist static energy budgets must be due to the export term, which is controlled by the large-scale vertical velocity profile.

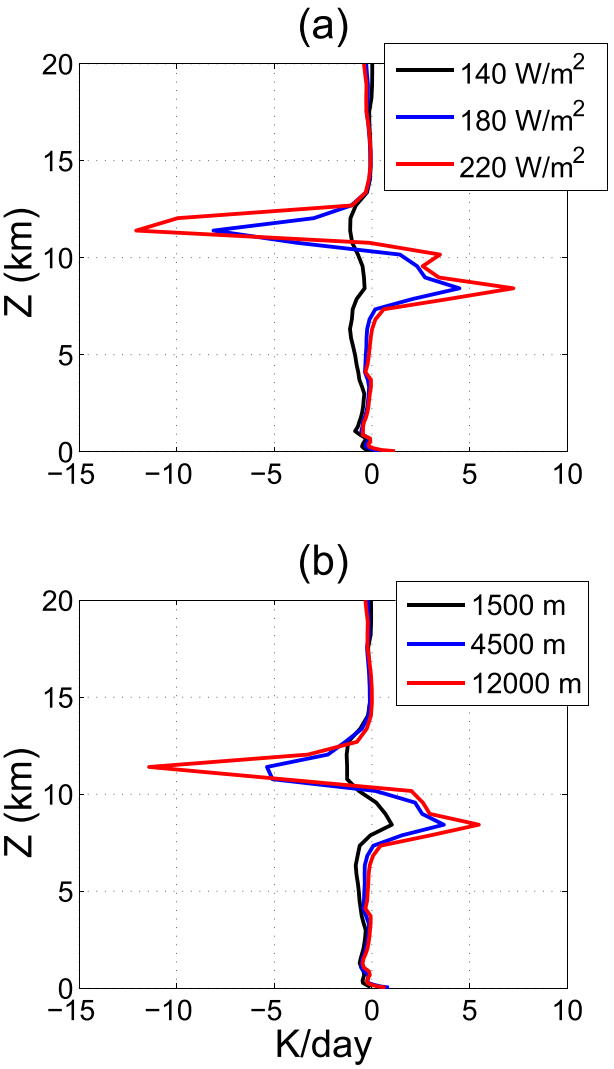

FIG. 2. Domain-averaged radiative heating profile as a function of (a) surface flux and (b) shear depth.

3. Results

Figure 3 shows time- and domain-averaged cloud fraction as a function of surface fluxes of 140, 180, and 220 W m^{-2} (Figs. 3a–c, respectively), in the unsheared environment, and shear depths of 1500, 4500, and 12 000 m (Figs. 3d–f, respectively), with intermediate surface fluxes, for interactive (solid) and prescribed (dashed) radiative heating. Cloud fraction is computed here as the fractional area at each level with total condensate (water and ice) mixing ratio greater than 0.005 g kg^{-1}. Cloud fraction in the upper troposphere increases with surface fluxes or shear-layer depth, approaching 100% for high surface fluxes and deep shear. We interpret this cloud layer as stratiform cloud. The increase in cloud fraction with surface fluxes or shear-layer

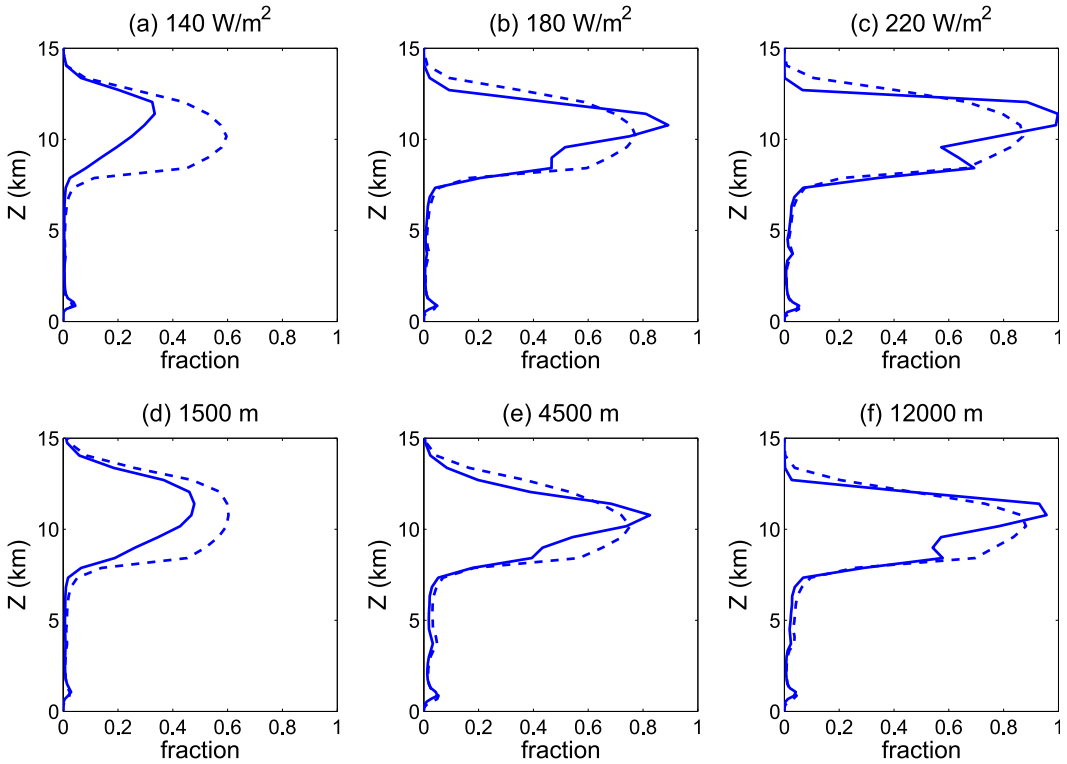

FIG. 3. Time-averaged cloud fraction for (a)–(c) different surface fluxes in an unsheared environment and (d)–(f) different shear depths at surface fluxes of 180 W m^{-2} from simulations with interactive (solid) and prescribed noninteractive (dashed) radiative heating.

depth is stronger for interactive than prescribed radiation. The two sets of experiments give similar cloud fraction profiles for intermediate and high surface fluxes and shear depths, but the interactive radiation has smaller cloud fraction for low surface fluxes and shallow shear.

Figure 4 shows time- and domain-averaged precipitation P (bullet symbols), as a function of surface fluxes in unsheared environment (Fig. 4a) and wind shear at the moderate surface flux value of 180 W m^{-2} (shear cases at low and high surface fluxes are similar and not shown; Fig. 4b), for experiments with interactive radiation (blue) and prescribed radiation (red). In all pairs of experiments, interactive radiation produces significantly less precipitation than does prescribed radiation. The difference monotonically increases with surface fluxes (Fig. 4a). The difference is about 1 mm day^{-1} for small surface fluxes and reaches 3 and 5 mm day^{-1} for the moderate and high surface fluxes, respectively, while remaining nearly constant with shear (Fig. 4b). Midlevel shear produces the greatest precipitation in both interactive and prescribed radiation experiments. A nonmonotonic relation between shear and precipitation was also found in the first part of this study, with specified radiative heating, and in other studies with different methodologies (e.g., Part I; Weisman and Rotunno 2004).

Precipitation is also diagnosed from the combined vertically integrated budgets of moist and dry static energy as (e.g., Sobel 2007; Wang and Sobel 2011)

$$P = \frac{1}{M}(L + H + \langle Q_R \rangle) - \langle Q_R \rangle - H, \qquad (2)$$

where L, H, $\langle Q_R \rangle$, and M are the latent heat flux, sensible heat flux, vertically integrated radiative heating, and normalized gross moist stability, respectively. The latter is defined as $M = \langle \overline{W}\,\overline{\partial h/\partial z} \rangle / \langle \overline{W}\,\overline{\partial s/\partial z} \rangle$, where W, s, and h are the large-scale vertical velocity and dry and moist static energy (MSE), respectively, angle brackets denote mass weighted vertical integrals, and overbars are domain and time mean. The above equation gives very good agreement with the model output as indicated in Fig. 4 with square symbols. The above equation helps us to interpret the causes of changes in P.

To understand the behavior of precipitation in the presence of cloud–radiation interaction, we look at the large-scale vertical motion W_{WTG}. Figure 5 shows the vertical profile of W_{WTG} with surface fluxes of 140, 180, and 220 W m^{-2} (Figs. 5a–c, respectively), in the unsheared

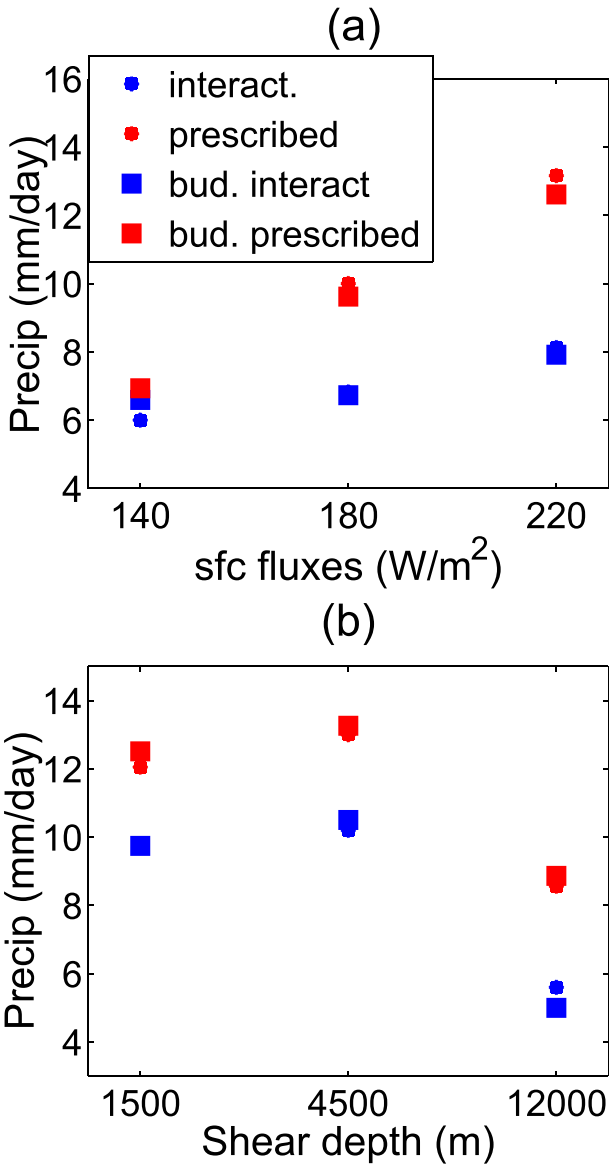

FIG. 4. Time-averaged surface precipitation as a function of (a) surface fluxes in an unsheared environment and (b) vertical wind shear depths at surface fluxes of 180 W m^{-2} for simulations of interactive (blue) and prescribed (red) radiation; bullets denote precipitation from model output and squares denote precipitation diagnosed from the moist and dry static energy budgets. Note the overlap between the bullets and the squares.

environment, and shear depths of 1500, 4500, and 12 000 m (Figs. 5d–f, respectively), with intermediate surface fluxes, for both interactive (solid curves) and prescribed (dashed) radiative heating. In all cases, when radiation is interactive the large-scale vertical motion exhibits a qualitatively similar vertical structure to that when radiation is prescribed, but with a stronger peak at about 10 km and slightly stronger subsidence in the lower levels (except in the shallow shear case; Fig. 5d), especially for the high surface flux and deep shear cases.

A closer look at the peak magnitude of the ascent and descent from Fig. 5 is shown in Fig. 6, which displays the maximum (Figs. 6a and 6c) and minimum (Figs. 6b and 6d) values of the W_{WTG} profile as a function of surface fluxes (Figs. 6a and 6b) and shear depth (Figs. 6c and 6d). The peak amplitude of the vertical motion is a monotonically increasing function of the surface fluxes and the shear depth for both interactive and prescribed radiative heating. However, there are significant differences between the two mean profiles, particularly at the highest surface fluxes and largest shear depth, where the maximum value from the interactive-radiation experiment significantly exceeds that from the prescribed radiation experiment. Though the upper-level cloud fraction in the high surface flux case is not significantly greater with than without interactive radiation (Fig. 3), the interactive radiation apparently acts in concert with the convection to strengthen the total upper-level heating, as apparent from the large-scale vertical motion profiles in Fig. 5 (recall that heating and large-scale vertical motion are directly related under WTG).

The change in the vertical motion profile induced by interactive radiation affects the column-integrated moist static energy budget. This indirect role of interactive radiation in the thermodynamics, as discussed in the introduction, can be usefully interpreted in terms of the normalized gross moist stability (e.g., Neelin and Held 1987; Sobel 2007; Raymond et al. 2009) shown in Fig. 7 and defined above as the export of moist static energy normalized by the export of dry static energy. Increasing surface fluxes while holding the radiative heating prescribed does not have a strong impact on M. For interactive radiation, however, as the surface fluxes increase, M increases strongly. Introduction of deep shear also increases M, and does so similarly whether radiation is fixed or interactive, but more when radiation is interactive. These increases are results of stronger ascent in the upper troposphere and slightly stronger descent in the lower troposphere (see Fig. 6), implying horizontal divergence both at upper levels and near the surface where moist static energy is large and convergence in midtroposphere where it is smaller. The value of M exceeds unity for the greatest surface fluxes and shear depth, meaning that the export of moist static energy exceeds the export of dry static energy, as seen late in the active phases of the MJO (e.g., Wang et al. 2015; Sobel et al. 2014). Any increase in radiative heating or surface fluxes for $M > 1$ is relatively inefficient in increasing precipitation since P is inversely proportional to the product of $1/M$ and these MSE sources [Eq. (2)].

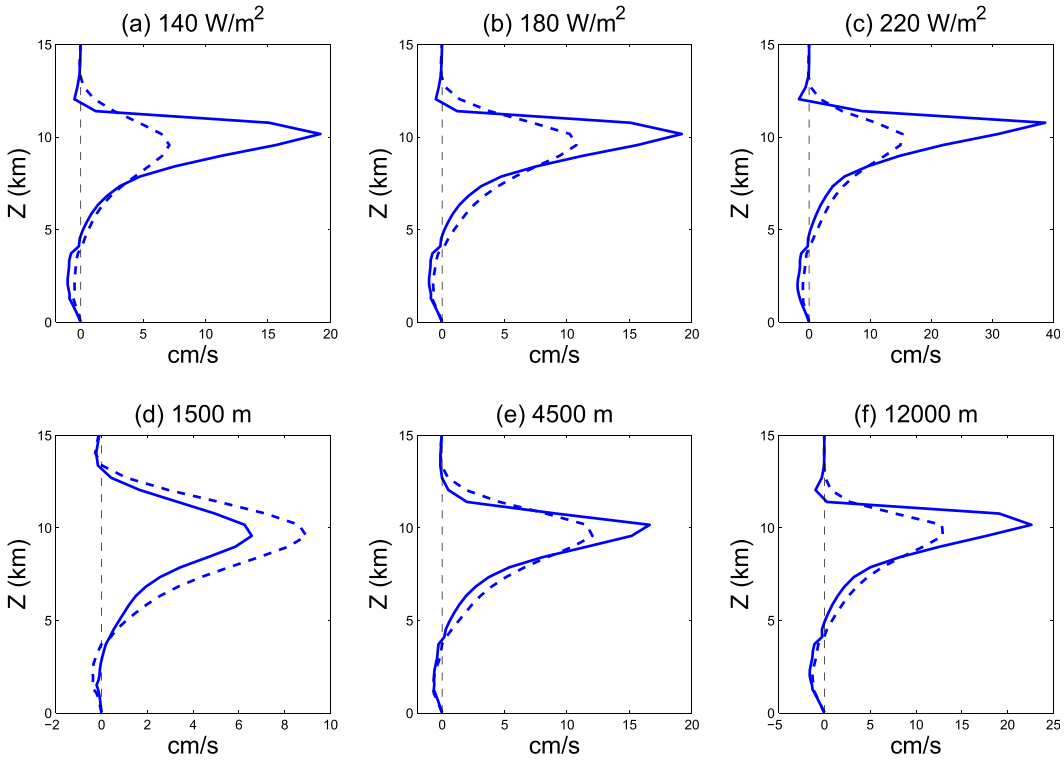

FIG. 5. Time-averaged large-scale vertical velocity for (a)–(c) different surface fluxes in an unsheared environment and (d)–(f) different shear depths at surface fluxes of 180 W m^{-2} for simulation of interactive (solid) and prescribed noninteractive (dashed) radiative profiles. Black dashed line marks zero vertical velocity. Note the change of the range in the x axes.

The strong increase in M in the interactive- versus fixed-radiation experiments implies some cancellation between direct and indirect effects of radiation in the moist static energy budgets of deep convective tropical disturbances, to the extent that (as we expect to be true in many cases) the tendency term is small enough that such disturbances are described to a reasonable approximation by Eq. (2) with appropriate averaging scales in space and time. In our simulations, the direct radiative feedback (defined operationally here as the horizontal-mean radiative heating change as a function of precipitation or other measure of convective activity) is present only implicitly, since interactive- and fixed-radiation experiments with the same surface fluxes share the same time-mean radiative heating profiles. We expect this direct feedback to be positive, increasing the radiative heating in the presence of large high cloud cover and column humidity and thus providing an anomalous source of MSE to the column. Our results imply that the radiative feedback also has a significant indirect effect that opposes this, changing the large-scale vertical motion profile so as to drive stronger advective export of MSE, thus acting as an anomalous sink of that quantity.

The result that the indirect radiative feedback increases moist static energy export may be relevant to a number of observed phenomena; one that occurs to us in particular is the MJO. As shown in several studies (e.g., Yasunaga and Mapes 2012; Kim et al. 2014; Sobel et al. 2014; Inoue and Back 2015a,b), the maximum in precipitation associated with the MJO active phase occurs nearly simultaneously with the maximum in column-integrated MSE over the Indian Ocean. Column-integrated vertical advection of MSE is negative (i.e., export; positive M) during the active phase and increases in magnitude as the phase advances, with minimum M before the peak MSE and precipitation and maximum after it (in either longitude or time). These variations in vertical advection are associated with the MJO's eastward propagation, as anomalous MSE import ahead acts to increase MSE leading up to the peak in the active phase, and anomalous export afterward acts to reduce it (e.g., Kiranmayi and Maloney 2011; Kim et al. 2014; Sobel et al. 2014; Inoue and Back 2015a,b; Yokoi and Sobel 2015).

The progression in the vertical motion profile to greater top-heaviness as the MJO's active phase matures is associated with a gradual transition from more convective to

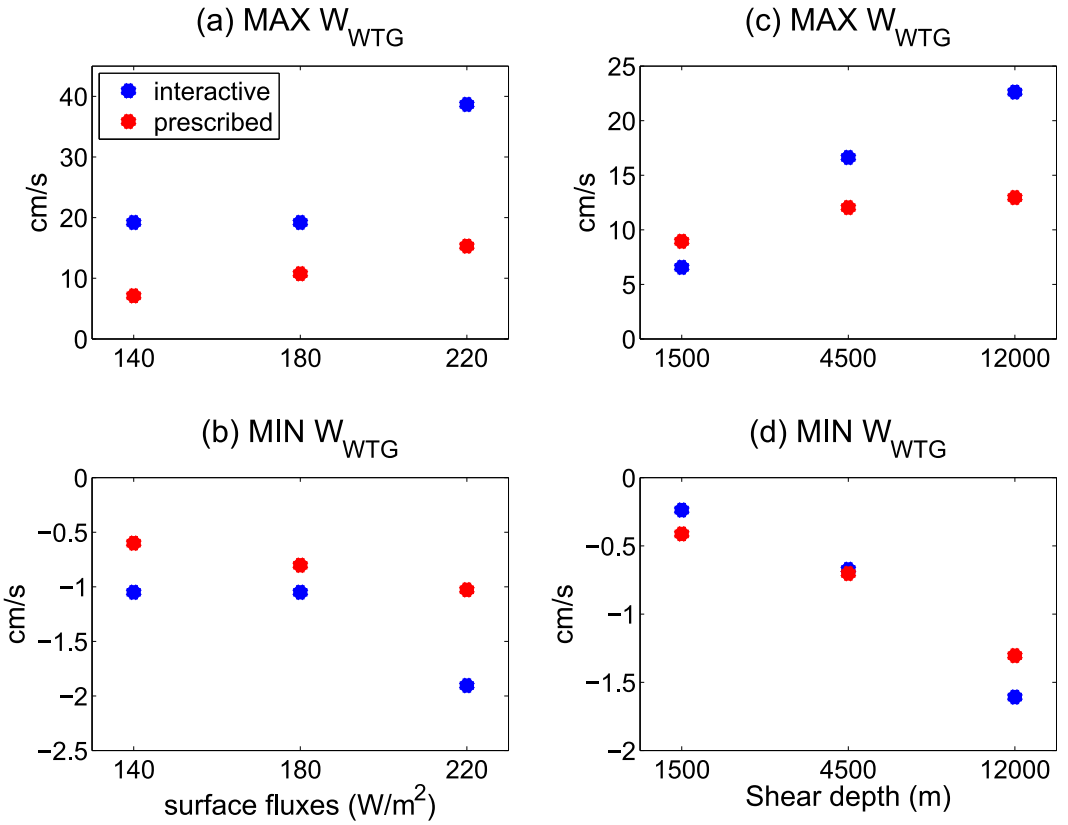

FIG. 6. Large-scale velocity of (a),(c) maximum ascending motion in the upper troposphere and (b),(d) descending motion in the lower troposphere for (a),(b) different surface fluxes in an unsheared environment and (c),(d) different shear depths at surface fluxes of 180 W m^{-2}. Simulations of interactive and prescribed noninteractive radiation are in blue and red, respectively.

more stratiform precipitation and cloud structures, similar to what happens in individual mesoscale systems, but on much larger scales in both space and time (Mapes et al. 2006). This is similar to the transition to greater stratiform cloudiness and more top-heavy large-scale vertical velocity shown as vertical shear or surface fluxes increase in Figs. 3 and 5. The larger surface fluxes or vertical shear can be thought of as representing the active phase, during which both surface fluxes and vertical shear are in fact observed to be larger than during the suppressed phase (e.g., Lin and Johnson 1996; Chen et al. 1996; Shinoda et al. 1998; Johnson and Ciesielski 2013; Sobel et al. 2014; de Szoeke et al. 2015). While the dynamics of the convective–stratiform transition are understood on the mesoscale, it has been unclear what mechanisms cause such a similar transition to play out on the planetary scale of the MJO, where it is not associated with individual mesoscale convective systems but rather a much larger envelope containing many such systems. While by no means solving this puzzle completely, our results suggest that both vertical shear and cloud–radiative interactions—both of which are strong in the late active phase of the MJO—may play key roles on this larger scale.

Finally, the temperature anomalies associated with interactive radiation are relevant to understanding the changes in vertical motion described above. Figure 8 shows the mean temperature anomalies from the RCE temperature profile as a function of surface fluxes (Fig. 8a) and shear depths (Fig. 8b). The low surface flux and shallow shear cases show warm anomalies throughout the atmosphere. However, as the surface fluxes or shear depth increase, the warm anomalies in the upper troposphere and cool anomalies in the lower troposphere both strengthen. These temperature anomaly profiles indicate a more stable environment, as usually observed in mesoscale convective systems and associated with horizontally extensive stratiform cloud and a second baroclinic mode component to the heating profile (Houze 1989). Greater stratiform cloud at larger surface fluxes or shear depth is indicated by Fig. 3, and top-heavier vertical motion profiles shown in Fig. 5 are consistent with this. We thus interpret the temperature changes as a response to greater

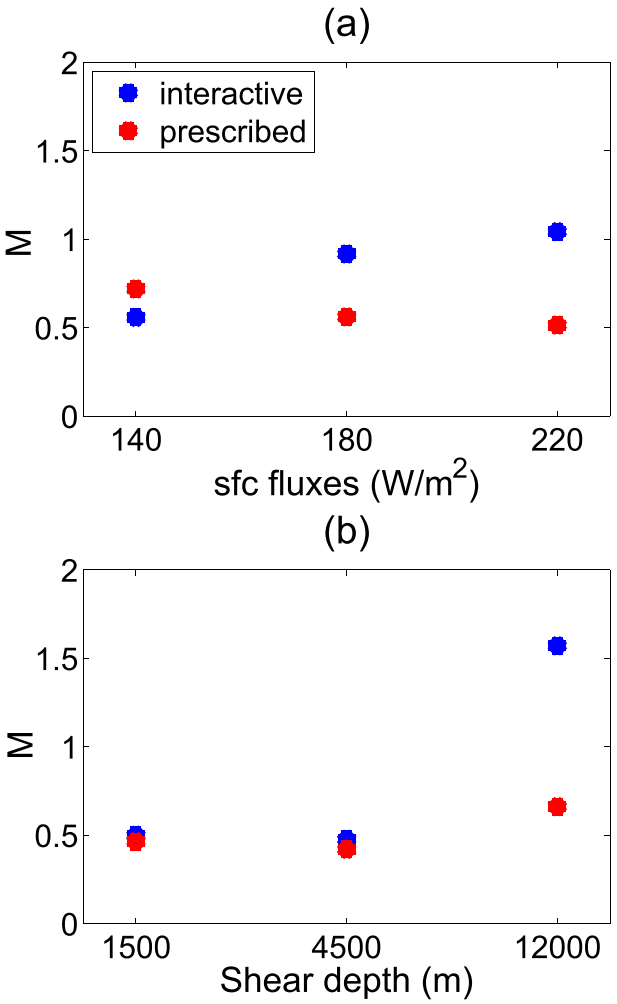

FIG. 7. Normalized gross moist stability as a function of (a) surface flux and (b) vertical wind shear depth for simulations of interactive (blue) and prescribed noninteractive (red) radiation.

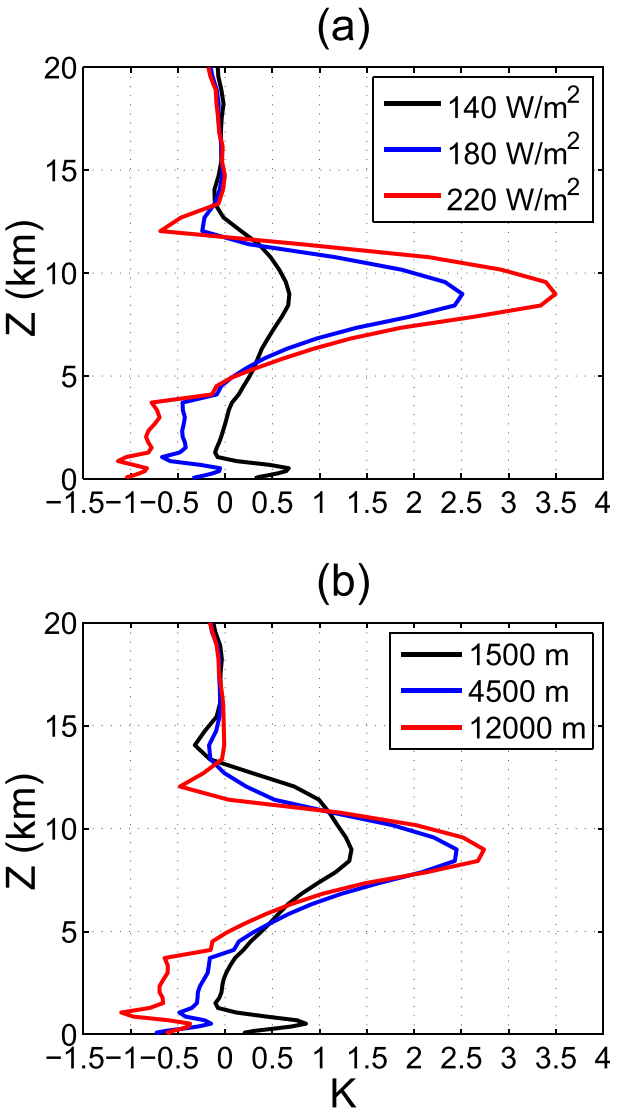

FIG. 8. Domain-mean profile of temperature anomalies, as a departure from RCE profile, as a function of (a) surface flux and (b) vertical shear depth.

stratiform cloudiness and precipitation as surface fluxes or shear depth increase.

4. Summary

We have presented results from idealized 3D cloud-resolving simulations with large-scale circulation parameterized under the weak temperature gradient approximation to investigate the effects of interactive radiation and vertical shear on tropical deep convection. Surface fluxes of heat and moisture were prescribed to remove wind–surface flux feedbacks, and results were presented for different imposed vertical wind shear profiles as well as different surface flux magnitudes. Results from simulations with fixed and interactive radiation were compared, with the two types of simulations having the same time-mean radiative heating profile so that any difference is only due to the interactivity itself. The direct radiative–convective feedback, associated with changes in the domain-averaged radiative heating profile (e.g., as a function of precipitation or column water vapor), was excluded.

Interactive radiation has a significant impact when surface fluxes are high in the presence of a substantial layer of high anvil cloud (Fig. 3). Interactions between radiation and convection increase the top-heaviness of the large-scale vertical motion profile and, consequently, increase the normalized gross moist stability and decrease mean precipitation, as moist static energy is more efficiently exported. Deep vertical shear has a similar effect; it has this effect with either fixed or

interactive radiation, but the reduction in precipitation is greatest when both deep shear and interactive radiation are present. We suggest that this behavior is relevant to the late active phase of the Madden–Julian oscillation (MJO) (Wang et al. 2015; Sobel et al. 2014), in which deep, strong vertical shear is present and surface fluxes are large. Coupling between radiation and dynamics of the type simulated here may be relevant to the increase in normalized gross moist stability, which is found in observations late in the active phase of the MJO (Kim et al. 2014; Sobel et al. 2014; Inoue and Back 2015a,b), and which plays a significant role in the MJO's eastward propagation.

Acknowledgments. This work was supported by NSF Grant AGS-1008847 and by the Office of Naval Research under MURI Grant N00014-12-1-0911. We acknowledge high-performance computing support from Yellowstone (ark:/85065/d7wd3xhc) provided by NCAR's Computational and Information Systems Laboratory, sponsored by the National Science Foundation. Special thanks to Prof. David Raymond and two anonymous reviewers for helpful comments.

REFERENCES

Anber, U., S. Wang, and A. Sobel, 2014: Response of atmospheric convection to vertical wind shear: Cloud-system-resolving simulations with parameterized large-scale circulation. Part I: Specified radiative cooling. *J. Atmos. Sci.*, **71**, 2976–2993, doi:10.1175/JAS-D-13-0320.1.

——, ——, and ——, 2015: Effect of surface fluxes versus radiative heating on tropical deep convection. *J. Atmos. Sci.*, **72**, 3378–3388, doi:10.1175/JAS-D-14-0253.1.

Bony, S., and K. A. Emanuel, 2005: On the role of moist processes in tropical intraseasonal variability: Cloud–radiation and moisture–convection feedbacks. *J. Atmos. Sci.*, **62**, 2770–2789, doi:10.1175/JAS3506.1.

Bretherton, C. S., and A. H. Sobel, 2002: A simple model of a convectively coupled Walker circulation using the weak temperature gradient approximation. *J. Climate*, **15**, 2907–2920, doi:10.1175/1520-0442(2002)015<2907:ASMOAC>2.0.CO;2.

——, P. N. Blossey, and M. Khairoutdinov, 2005: An energy-balance analysis of deep convective self-aggregation above uniform SST. *J. Atmos. Sci.*, **62**, 4273–4292, doi:10.1175/JAS3614.1.

Bu, Y. P., R. G. Fovell, and K. L. Corbosiero, 2014: Influence of cloud–radiative forcing on tropical cyclone structure. *J. Atmos. Sci.*, **71**, 1644–1662, doi:10.1175/JAS-D-13-0265.1.

Chen, S. S., R. A. Houze Jr., and B. E. Mapes, 1996: Multiscale variability of deep convection in relation to large-scale circulation in TOGA COARE. *J. Atmos. Sci.*, **53**, 1380–1409, doi:10.1175/1520-0469(1996)053<1380:MVODCI>2.0.CO;2.

Chikira, M., 2014: Eastward-propagating intraseasonal oscillation represented by Chikira–Sugiyama cumulus parameterization. Part II: Understanding moisture variation under weak temperature gradient balance. *J. Atmos. Sci.*, **71**, 615–639, doi:10.1175/JAS-D-13-038.1.

Collins, W. D., and Coauthors, 2004: Description of the NCAR Community Atmosphere Model: CAM3.0. NCAR Tech. Rep. NCAR/TN-464+STR, 226 pp. [Available online at http://www.cesm.ucar.edu/models/atm-cam/docs/description/description.pdf.]

de Szoeke, S. P., J. B. Edson, J. R. Marion, C. W. Fairall, and L. Bariteau, 2015: The MJO and air–sea interaction in TOGA COARE and DYNAMO. *J. Climate*, **28**, 597–622, doi:10.1175/JCLI-D-14-00477.1.

Emanuel, K., A. A. Wing, and E. M. Vincent, 2014: Radiative-convective instability. *J. Adv. Model. Earth Syst.*, **6**, 75–90, doi:10.1002/2013MS000270.

Grabowski, W. W., and M. W. Moncrieff, 2002: Large-scale organization of tropical convection in two-dimensional explicit numerical simulations: Effects of interactive radiation. *Quart. J. Roy. Meteor. Soc.*, **128**, 2349–2375, doi:10.1256/qj.01.104.

Hakim, G. J., 2013: The variability and predictability of axisymmetric hurricanes in statistical equilibrium. *J. Atmos. Sci.*, **70**, 993–1005, doi:10.1175/JAS-D-12-0188.1.

Hartmann, D. L., L. A. Moy, and Q. Fu, 2001: Tropical convection and the energy balance at the top of the atmosphere. *J. Climate*, **14**, 4495–4511, doi:10.1175/1520-0442(2001)014<4495:TCATEB>2.0.CO;2.

Houze, R. A., Jr., 1989: Observed structure of mesoscale convective systems and implications for large-scale heating. *Quart. J. Roy. Meteor. Soc.*, **115**, 425–461, doi:10.1002/qj.49711548702.

Inoue, K., and L. E. Back, 2015a: Column-integrated moist static energy analysis on various time scales during TOGA COARE. *J. Atmos. Sci.*, **72**, 1856–1871, doi:10.1175/JAS-D-14-0249.1.

——, and ——, 2015b: Gross moist stability assessment during TOGA COARE: Various interpretations of gross moist stability. *J. Atmos. Sci.*, **72**, 4148–4166, doi:10.1175/JAS-D-15-0092.1.

Johnson, R. H., and P. E. Ciesielski, 2013: Structure and properties of Madden–Julian oscillations deduced from DYNAMO sounding arrays. *J. Atmos. Sci.*, **70**, 3157–3179, doi:10.1175/JAS-D-13-065.1.

Kim, D., A. H. Sobel, and I.-S. Kang, 2011: A mechanism denial study on the Madden-Julian oscillation. *J. Adv. Model. Earth Syst.*, **3**, M12007, doi:10.1029/2011MS000081.

——, J.-S. Kug, and A. H. Sobel, 2014: Propagating vs. nonpropagating Madden–Julian oscillation events. *J. Climate*, **27**, 111–125, doi:10.1175/JCLI-D-13-00084.1.

Kiranmayi, L., and E. D. Maloney, 2011: Intraseasonal moist static energy budget in reanalysis data. *J. Geophys. Res.*, **116**, D21117, doi:10.1029/2011JD016031.

Lin, J.-L., and B. E. Mapes, 2004: Radiation budget of the tropical intraseasonal oscillation. *J. Atmos. Sci.*, **61**, 2050–2062, doi:10.1175/1520-0469(2004)061<2050:RBOTTI>2.0.CO;2.

Lin, X., and R. H. Johnson, 1996: Kinematic and thermodynamic characteristics of the flow over the western Pacific warm pool during TOGA COARE. *J. Atmos. Sci.*, **53**, 695–715, doi:10.1175/1520-0469(1996)053<0695:KATCOT>2.0.CO;2.

Mapes, B., S. Tulich, J. Lin, and P. Zuidema, 2006: The mesoscale convection life cycle: Building block or prototype for large-scale tropical waves? *Dyn. Atmos. Oceans*, **42**, 3–29, doi:10.1016/j.dynatmoce.2006.03.003.

Neelin, J. D., and I. M. Held, 1987: Modeling tropical convergence based on the moist static energy budget. *Mon. Wea. Rev.*, **115**, 3–12, doi:10.1175/1520-0493(1987)115<0003:MTCBOT>2.0.CO;2.

Ramanathan, V., R. D. Cess, E. F. Harrison, P. Minnis, B. R. Barkstrom, E. Ahmad, and D. Hartmann, 1989: Cloud-radiative forcing and climate: Results from the Earth Radiation

Budget Experiment. *Science*, **243**, 57–63, doi:10.1126/science.243.4887.57.

Raymond, D. J., 2001: A new model of the Madden–Julian oscillation. *J. Atmos. Sci.*, **58**, 2807–2819, doi:10.1175/1520-0469(2001)058<2807:ANMOTM>2.0.CO;2.

——, and X. Zeng, 2005: Modelling tropical atmospheric convection in the context of the weak temperature gradient approximation. *Quart. J. Roy. Meteor. Soc.*, **131**, 1301–1320, doi:10.1256/qj.03.97.

——, S. L. Sessions, A. H. Sobel, and Ž. Fuchs, 2009: The mechanics of gross moist stability. *J. Adv. Model. Earth Syst.*, **1** (9), doi:10.3894/JAMES.2009.1.9.

Shinoda, T., H. H. Hendon, and J. Glick, 1998: Intraseasonal variability of surface fluxes and sea surface temperature in the tropical western Pacific and Indian Oceans. *J. Climate*, **11**, 1685–1702, doi:10.1175/1520-0442(1998)011<1685:IVOSFA>2.0.CO;2.

Sobel, A. H., 2007: Simple models of ensemble-averaged tropical precipitation and surface wind, given the sea surface temperature. *The Global Circulation of the Atmosphere*, T. Schneider and A. H. Sobel, Eds., Princeton University Press, 219–251.

——, and C. S. Bretherton, 2000: Modeling tropical precipitation in a single column. *J. Climate*, **13**, 4378–4392, doi:10.1175/1520-0442(2000)013<4378:MTPIAS>2.0.CO;2.

——, and H. Gildor, 2003: A simple time-dependent model of SST hot spots. *J. Climate*, **16**, 3978–3992, doi:10.1175/1520-0442(2003)016<3978:ASTMOS>2.0.CO;2.

——, and E. D. Maloney, 2013: Moisture modes and the eastward propagation of the MJO. *J. Atmos. Sci.*, **70**, 187–192, doi:10.1175/JAS-D-12-0189.1.

——, S. Wang, and D. Kim, 2014: Moist static energy budget of the MJO during DYNAMO. *J. Atmos. Sci.*, **71**, 4276–4291, doi:10.1175/JAS-D-14-0052.1.

Su, H., and J. D. Neelin, 2002: Teleconnection mechanisms for tropical Pacific descent anomalies during El Nino. *J. Atmos. Sci.*, **59**, 2694–2712, doi:10.1175/1520-0469(2002)059<2694:TMFTPD>2.0.CO;2.

Tobin, I., S. Bony, C. E. Holloway, J.-Y. Grandpeix, G. Sèze, D. Coppin, S. J. Woolnough, and R. Roca., 2013: Does convective aggregation need to be represented in cumulus parameterizations? *J. Adv. Model. Earth Syst.*, **5**, 692–703, doi:10.1002/jame.20047.

Wang, S., and A. H. Sobel, 2011: Response of convection to relative sea surface temperature: Cloud-resolving simulations in two and three dimensions. *J. Geophys. Res.*, **116**, D11119, doi:10.1029/2010JD015347.

——, ——, F. Zhang, Y. Q. Sun, Y. Yue, and L. Zhou, 2015: Regional simulation of the October and November MJO events observed during the CINDY/DYNAMO field campaign at gray zone resolution. *J. Climate*, **28**, 2097–2119, doi:10.1175/JCLI-D-14-00294.1.

Weisman, M. L., and R. Rotunno, 2004: ''A theory for strong long-lived squall lines'' revisited. *J. Atmos. Sci.*, **61**, 361–382, doi:10.1175/1520-0469(2004)061<0361:ATFSLS>2.0.CO;2.

Wing, A. A., and K. A. Emanuel, 2014: Physical mechanisms controlling self-aggregation of convection in idealized numerical modeling simulations. *J. Adv. Model. Earth Syst.*, **6**, 59–74, doi:10.1002/2013MS000269.

Yasunaga, K., and B. E. Mapes, 2012: Differences between more divergent vs. more-rotational types of convectively coupled equatorial waves. Part I: Space–time spectral analyses. *J. Atmos. Sci.*, **69**, 3–16, doi:10.1175/JAS-D-11-033.1.

Yokoi, S., and A. H. Sobel, 2015: Intraseasonal variability and seasonal march of the moist static energy budget over the eastern Maritime Continent during CINDY2011/DYNAMO. *J. Meteor. Soc. Japan*, doi:10.2151/jmsj.2015-041, in press.